The Drop Size in Membrane Emulsification Determined from the Balance of Capillary and Hydrodynamic Forces†

Nikolay C. Christov, Krassimir D. Danov, Darina K. Danova,‡ and Peter A. Kralchevsky*

Laboratory of Chemical Physics and Engineering, Faculty of Chemistry, University of Sofia, 1164 Sofia, Bulgaria

Received July 30, 2007. In Final Form: September 7, 2007

Here, we investigate experimentally and theoretically the factors that determine the size of the emulsion droplets produced by membrane emulsification in "batch regime" (without applied crossflow). Hydrophilic glass membranes of pore diameters between 1 and 10 μm have been used to obtain oil-in-water emulsions. The working surfactant concentrations are high enough to prevent drop coalescence. Under such conditions, the size of the formed drops does not depend on the surfactant type and concentration, on the interfacial tension, or on the increase of viscosity of the inner (oil) phase. The drops are monodisperse when the working transmembrane pressure is slightly above the critical pressure for drop breakup. At higher pressures, the size distribution becomes bimodal: a superposition of a "normal" peak of monodisperse drops and an "anomalous" peak of polydisperse drops is observed. The theoretical model assumes that, at the moment of breakup, the hydrodynamic ejection force acting on the drop is equal to the critical capillary force that corresponds to the stability−instability transition in the drop shape. The derived equations are applied to predict the mean size of the obtained drops in regimes of constant flow rate and constant transmembrane pressure. Agreement between theory and experiment is established for the latter regime, which corresponds to our experimental conditions. The transition from unimodal to bimodal drop size distribution upon increase of the transmembrane pressure can be interpreted in terms of the transition from "dripping" to "jetting" mechanisms of drop detachment.

1. Introduction

The method of membrane emulsification has found broad applications in many fields in which the production of monodisperse emulsions is needed. One of them is for the fabrication of monodisperse colloidal particles: silica-hydrogel and polymer microspheres, porous and cross-linked polymer particles, microspheres containing carbon black for toners, and so forth. In the food industry, the method has been used for obtaining oil-in-water (O/W) emulsions (e.g., dressings, artificial milk, cream liqueurs) and for the preparation of some water-in-oil (W/O) emulsions (e.g., margarine and low-fat spreads). A third field is the production of multiple emulsions and microcapsules with applications in pharmacy and chemotherapy. Detailed information can be found in recently published review articles.[1−6] Closely related to membrane emulsification is the method employing capillary tubes or microchannels to produce monodisperse emulsions.[7−9]

The key problem of membrane emulsification is related to the explanation and prediction of the drop size as a function of the system's parameters: pore diameter, surfactant type and concentration, interfacial tension, viscosity of the oil and water phases, and applied transmembrane pressure and crossflow in the continuous phase. Different approaches have been used to solve this problem: regression analysis of experimental data,[9] modeling of the drop expansion and surfactant adsorption by a surface evolver,[10,11] three-dimensional computational fluid dynamics simulations,[12,13] and lattice Boltzmann simulations.[14] The quantitative theoretical analysis demands one to determine the forces exerted on the growing emulsion drop and to establish the mechanism of drop detachment from the pores.

In a preceding work,[15] we developed a quantitative theory of the hydrodynamic forces that are acting on the forming drop in the absence of crossflow in the continuous phase. These experimental conditions correspond to the "batch method" (Figure 1). The understanding and quantitative description of the processes in this simpler case represent a necessary step toward the analysis of the more complicated case when crossflow is present.

The flow of the disperse phase through the capillary, as it inflates the droplet, engenders a hydrodynamic ejection force that tends to detach the droplet from the pore.[15,16] The hydrodynamic theory shows that, under typical experimental conditions, this process happens at small Reynolds numbers, for which the inertial terms in the Navier−Stokes equation are negligible.[15] Hence, under such conditions, the ejection force

† Part of the Molecular and Surface Forces special issue.

* Corresponding author. Phone: (+359) 2-962 5310. Fax: (+359) 2-962 5438. E-mail: pk@lcpe.uni-sofia.bg.

‡ Present address: Division of Physics and Astronomy, Vrije Universiteit Amsterdam, 1081HV Amsterdam, The Netherlands.

(1) Schröder, V.; Schubert, H. *Colloids Surf., A* **1999**, *152*, 103−109.
(2) Joscelyne, S. M.; Trägårdh, G. *J. Membr. Sci.* **2000**, *169*, 107−117.
(3) Christov, N. C.; Ganchev, D. N.; Vassileva, N. D.; Denkov, N. D.; Danov, K. D.; Kralchevsky, P. A. *Colloids Surf., A* **2002**, *209*, 83−104.
(4) Charcosset, C.; Limayem, I.; Fessi, H. *J. Chem. Technol. Biotechnol.* **2004**, *79*, 209−218.
(5) Vladislavljević, G. T.; Williams, R. A. *Adv. Colloid Interface Sci.* **2005**, *113*, 1−20.
(6) Lambrich, U.; Schubert, H. *J. Membrane Sci.* **2005**, *257*, 76−84.
(7) Kawakatsu, T.; Kikuchi, Y.; Nakajima, M. *J. Am. Oil Chem. Soc.* **1997**, *74*, 317−321.
(8) Sugiura, S.; Nakajima, M.; Seki, M. *Langmuir* **2002**, *18*, 5708−5712.
(9) Sugiura, S.; Nakajima, M.; Seki, M. *Langmuir* **2002**, *18*, 3854−3859.
(10) Rayner, M.; Trägårdh, G.; Trägårdh, C.; Dejmek, P. *J. Colloid Interface Sci.* **2004**, *279*, 175−185.
(11) Rayner, M.; Trägårdh, G.; Trägårdh, C. *Colloids Surf., A* **2005**, *266*, 1−17.
(12) Kobayashi, I.; Mukataka, S.; Nakajima, M. *Langmuir* **2004**, *20*, 9868−9877.
(13) Kobayashi, I.; Mukataka, S.; Nakajima, M. *Langmuir* **2005**, *21*, 5722−5730.
(14) van der Graaf, S.; Nisisako, T.; Schroën, C. G. P. H.; van der Sman, R. G. M.; Boom, R. M. *Langmuir* **2006**, *22*, 4144−4152.
(15) Danov, K. D.; Danova, D. K.; Kralchevsky, P. A. *J. Colloid Interface Sci.* **2008**, doi: 10.1016/j.jcis.2007.08.061.
(16) Schröder, V.; Behrend, O.; Schubert, H. *J. Colloid Interface Sci.* **1998**, *202*, 334−340.

10.1021/la702306f CCC: $40.75
Published on Web 10/27/2007

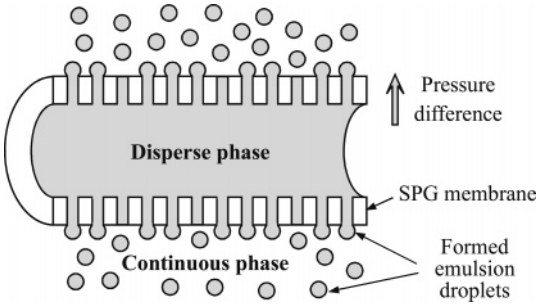

Figure 1. Sketch of the used membrane emulsification method. The disperse (oil) phase is supplied under pressure in a tubular microporous glass membrane, and the emulsion drops appear at the outer surface of the membrane, which is immersed in the continuous (water) phase (batch method).

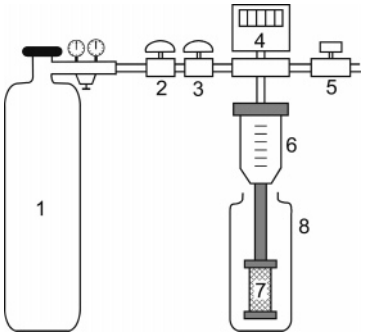

Figure 2. Sketch of the membrane-emulsification setup: (1) gas bottle; (2) and (3) needle valves; (4) pressure gauge; (5) vent valve; (6) container filled with the disperse phase (oil); (7) emulsification membrane (Figure 1); (8) container for the produced emulsion.

has a predominantly viscous (rather than inertial) character. This force was expressed in terms of three universal functions of the drop diameter, which have been computed numerically, and interpolation formulas have been obtained for their easier calculation.[15]

In the present study, we apply the results for the hydrodynamic forces from ref 15 to predict the size of the drops produced by membrane emulsification. First, we present new experimental data for the effects produced by various factors: surfactant type and concentration, interfacial tension, viscosities of disperse and continuous phases, pore size, and transmembrane pressure (sections 2−4). Next, the theory from ref 15 is upgraded by the formulation of a quantitative criterion for drop detachment from the membrane (section 5.2). This criterion is utilized to derive expressions for the mean drop size under conditions of constant flow rate (section 5.3) and constant transmembrane pressure (section 5.4). Finally, the theoretical expressions are applied to interpret the experimental data and to identify the main factors and effects that determine the drop-size distributions in the investigated emulsions (sections 5.5 and 6).

2. Materials and Methods

2.1. Membrane Emulsification Setup and Procedure. In our experiments, we used a Microkit membrane emulsification module (SPG Technology, Miyazaki, Japan), which works with conventional tubular type Shirasu porous glass (SPG) membranes of outer diameter 10 mm, thickness 1 mm, and working area of approximately 3 cm^2 (see ref 17 about the conventional and novel types of SPG membranes). Membranes of different average pore diameter can be used, from 0.1 to 20 μm. The porosity, that is, the surface fraction of the pores, is about 50% according to the manufacturer. The working pressure difference is up to 300 kPa. As the membranes are made of hydrophilic glass, they are suitable for producing O/W emulsions, which is the type of emulsions we are investigating. All experiments were carried out at temperature $T = 23 \pm 2$ °C. (After hydrophobization, the membranes can also be used for obtaining W/O emulsions.)

To produce O/W emulsions, the oil phase is supplied inside the tubular membrane, and the oil drops are released in the outer aqueous phase (Figure 1). The higher pressure in the oil is provided by a gas (nitrogen) bottle. The only directed motion of the formed oil droplets in the water phase occurs under the action of the buoyancy force. There is no applied crossflow (batch method).[18] The experimental setup is sketched in Figure 2.

In the beginning of each experiment, the tubular membrane is first fixed at the holder of the emulsification setup and immersed in the aqueous surfactant solution. Then, the oily phase is supplied under pressure. We start with an initial pressure that is insufficiently high for the oil to displace the aqueous phase from the pores of the membrane, and, consequently, emulsification is not observed. Next, the pressure is gradually and slowly increased until the emulsification begins at a certain critical (threshold) pressure, P_{cr}.[19] To investigate the effect of the applied transmembrane pressure, P, on the size of the produced emulsion drops, we varied P in a certain range above P_{cr} (see section 4.5). In these experiments, the values of the critical pressure, P_{cr}, were different because of the different interfacial tensions, γ, and pore diameters, d_p. After the end of each emulsification experiment, the used membrane was recovered by means of a procedure that is described in ref 3.

2.2. Materials. To investigate the effect of viscosity of the disperse phase, η_a, on the size of produced emulsion droplets, we used oils of different viscosities: *n*-hexadecane, soybean oil (SBO), and silicone oil, with viscosities, η_a, of 3, 50, and 500 mPa·s, respectively. The *n*-hexadecane ($C_{16}H_{34}$), a product of Sigma, was used without additional purification. The SBO was purified by passing through a glass column filled with the chromatographic adsorbent Florisil (Fluka). The silicone oil was poly(dimethylsiloxane) (PDMS) DC 200 (Fluka) of viscosity 500 mPa·s.

Four surfactants were used as emulsifiers in different series of experiments: sodium dodecyl sulfate (SDS, Acros Organics), sodium dodecyl benzene sulfonate (SDBS, Aldrich, technical grade); sodium bis(2-ethyl-1-hexyl) sulfosuccinate (AOT, Sigma), and the zwitterionic surfactant cocamidopropyl betaine (CAPB, commercial name "Tego Betaine F50", Goldschmidt Chemical Co., McDonald, PA). We did not use cationic surfactants because they could adsorb on the glass membrane, hydrophobize it, and create problems when producing O/W emulsions.

All aqueous solutions were prepared with deionized water from a Milli-Q Organex system (Millipore). Some of the solutions also contained NaCl (Merck, GR for analysis). The viscosity of the used surfactant solutions was very close to the viscosity of pure water, $\eta_b = 0.9$ mPa·s. In a series of experiments, to increase the viscosity of the aqueous phase, η_b, we used surfactant solutions with added 62 wt % glycerol, whose viscosity is $\eta_b = 11$ mPa·s.[20] For this purpose, we used anhydrous glycerol from Sigma (ACS reagent-grade purity).

2.3. Measurements of Drop Diameters. Representative samples of the produced emulsions were observed in transmitted light by a Zeiss Axioplan microscope with objectives ×100, ×50, and ×20. The specimens were prepared by placing a small portion of the emulsion in a cytometric glass cell (large ratio rectangle capillaries, 0.2 × 4 mm). The microscopic pictures were recorded by means of a CCD camera and digital memory VCR (Panasonic WV-5490). The images were processed by using semiautomatic image analysis software, operating with a Targa+ graphic board (True Vision, USA). To determine the diameter of a given emulsion drop, at the computer

(17) Kukizaki, M., Goto, M. *J. Membr. Sci.* **2007**, *299*, 190−199.

(18) Kandori, K. In *Food Processing: Recent Developments*; Gaonkar, A. G., Ed.; Elsevier: Amsterdam, 1995; pp 113−142.

(19) Nakashima, T., Shimizu, M., Kukizaki, M., Eds. *Membrane Emulsification Operational Manual*, 1st ed.; Department of Chemistry, Industrial Research Institute of Miyazaki Prefecture: Miyazaki, Japan, 1991.

(20) See http://www.dow.com/glycerine/resources/viscosity.htm for the viscosity of aqueous glycerol solutions.

screen, a circle of variable size is adjusted at the drop periphery, and after that the diameter of the circle is automatically recorded by the computer program. To obtain the drop-size distribution for a given emulsion, the diameters of several thousand droplets (at least 1000) were measured. All droplets in a given frame were taken into account, even the smallest ones that were still visible. In our experiments, the lower limit for the measurement of drop diameter was about 0.8 μm.

3. Statistical Analysis of Drop Size Data

3.1. Theoretical Background. Our purpose is to compare the mean drop diameter predicted by the theoretical model (section 5) with the experimental mean diameter. For this goal, from the experimental data we determined the mean diameter by drop number (rather than by drop volume or surface area). The applied statistical analysis is outlined below.

First, the diameters of a set of N emulsion droplets, measured as explained in section 2.3, are ordered in an ascending series, d_1, d_2, ..., d_K, where K is the total number of different drop diameters. Each drop diameter, d_k, appears n_k times in the original data set, $k = 1, 2, ..., K$. (For example, if we have measured the diameters of 1000 drops, it could happen that four different drops have diameter $d_k = 6.7$ μm; then, we set $n_k = 4$.) The total number of drops is

$$N = \sum_{k=1}^{K} n_k \tag{3.1}$$

By definition, the *cumulative function*, $f(d_k)$, is equal to the number of drops whose diameter is $d \le d_k$; the function $f(d_k)$ is normalized by the total drop number, N:[21,22]

$$f(d_k) = \frac{1}{N}\sum_{j=1}^{k} n_j \tag{3.2}$$

By means of eq 3.2, one can calculate $f(d_k)$ for each experimentally measured drop diameter, d_k. We found that the experimental data obey the *lognormal distribution*. Its probability function is[21,22]

$$p(d) = \frac{1}{\sqrt{2\pi}}\frac{1}{\ln \sigma}\exp\left[-\frac{\ln^2(d/d_d)}{2\ln^2 \sigma}\right], (d > 0) \tag{3.3}$$

Here, d_d is the mean diameter, and σ is a dimensionless dispersion ($\sigma > 1$). The peak of $p(d)$ defined in eq 3.3 is non-symmetric. The diameters of 50% of the drops belong to the interval $d_d/\sigma \le d \le d_d\sigma$ that characterizes the drop polydispersity. In the limiting case $\sigma \to 1$, one can expand in series the logarithms in eq 3.3 and keep the leading terms; then, eq 3.3 reduces to the normal (Gaussian) distribution.[21,22]

The cumulative function, $f(d)$, which corresponds to the lognormal distribution, (eq 3.3) is

$$f(d) \equiv \int_{-\infty}^{\ln d} p(\hat{d})\mathrm{d}(\ln \hat{d}) = \frac{1}{2}[1 + \mathrm{erf}(y)] \tag{3.4}$$

$$y \equiv \frac{\ln(d/d_d)}{\sqrt{2}\ln \sigma} \tag{3.5}$$

where $\hat{d}$ is an integration variable, and erf(y) is the error function.[23] We fitted the experimental function $f(d_k)$ (eq 3.2) by means of the theoretical dependence $f(d)$ given by eq 3.4, and determined d_d and σ as adjustable parameters (see Figure 3 and section 3.2).

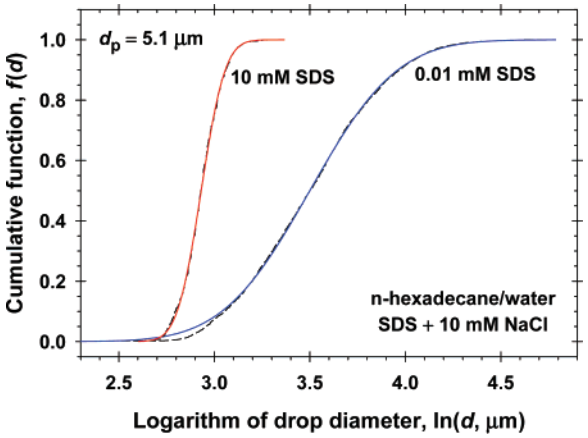

Figure 3. Plot of the cumulative function, f, vs the logarithm of drop diameter, ln(d), where d is given in micrometers, for two concentrations of SDS (0.01 mM and 10 mM) in the aqueous phase that also contains 10 mM NaCl. The experimental dashed lines, obtained from eq 3.2, coincide almost everywhere with the theoretical solid lines, which represent fits by means of eqs 3.4 and 3.5.

In some cases, the experimental drop-size distribution is bimodal (with two peaks, see below). In such cases, the data can be described by the *bimodal lognormal distribution*:[21,22]

$$p(d) = \frac{1}{\sqrt{2\pi}}\frac{1-\beta}{\ln \sigma_1}\exp\left[-\frac{\ln^2(d/d_{d1})}{2\ln^2 \sigma_1}\right] + \frac{1}{\sqrt{2\pi}}\frac{\beta}{\ln \sigma_2}\exp\left[-\frac{\ln^2(d/d_{d2})}{2\ln^2 \sigma_2}\right] \tag{3.6}$$

A comparison of eqs 3.3 and 3.6 indicates that the bimodal distribution represents a superposition of two different unimodal lognormal distributions with probabilities $1-\beta$ and β, mean diameters d_{d1} and d_{d2}, and dimensionless dispersions σ_1 and σ_2. The cumulative function $f(d)$ corresponding to the bimodal lognormal distribution (eq 3.6) is

$$f(d) \equiv \int_{-\infty}^{\ln d} p(\hat{d})\mathrm{d}(\ln \hat{d}) = \frac{1-\beta}{2}[1 + \mathrm{erf}(y_1)] + \frac{\beta}{2}[1 + \mathrm{erf}(y_2)] \tag{3.7}$$

$$y_j \equiv \frac{\ln(d/d_{dj})}{\sqrt{2}\ln \sigma_j} (j = 1, 2) \tag{3.8}$$

In the case of bimodal drop-size distribution, we fitted the experimental function $f(d_k)$ (eq 3.2) by means of the theoretical dependence $f(d)$ given by eq 3.7, and determined d_{d1}, d_{d2}, σ_1, and σ_2 as adjustable parameters (see below).

3.2. Illustrative Examples. *(a) Unimodal Distributions.* Figure 3 shows typical experimental cumulative functions (dashed lines) and their fits by means of the lognormal cumulative function (solid lines) (eq 3.4). The agreement between the theoretical and experimental cumulative functions is so good that the dashed and solid lines coincide almost everywhere (Figure 3). The respective experimental data are obtained for *n*-hexadecane-in-water emulsions that have been produced by means of membrane emulsification (section 2) using an SPG membrane of average pore diameter $d_p = 5.1$ μm. The aqueous phase is a solution of

(21) Box, G. E. P.; Hunter, J. S.; Hunter, W. G. *Statistics for Experiments: Design, Innovation, and Discovery*, 2nd ed.; Wiley: Hoboken, NJ, 2005.

(22) Crow, E. L., Shimizu, K., Eds. *Lognormal Distributions: Theory and Applications*; Marcel Dekker: New York, 1988.

(23) Korn, G. A.; Korn, T. M. *Mathematical Handbook*; McGraw-Hill: New York, 1968.

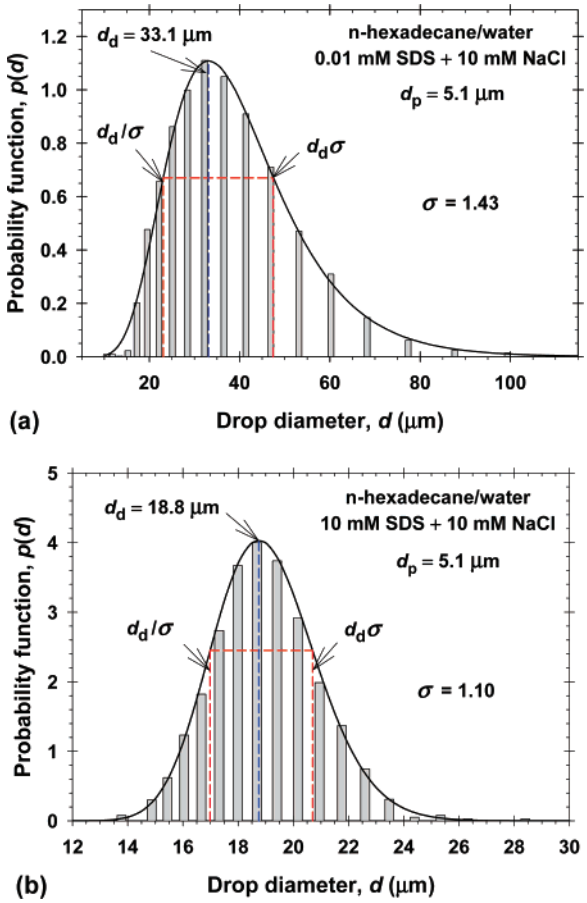

Figure 4. Plots of the probability function, $p(d)$ (the solid lines), which are calculated from eq 3.3 using parameter values determined from the fits of the cumulative functions by lognormal distribution (Figure 3). The aqueous phase contains (a) 0.01 mM SDS + 10 mM NaCl and (b) 10 mM SDS + 10 mM NaCl. The bar chart represents the histogram of the experimental drop size distribution; d_d is the mean drop diameter; σ is the dimensionless dispersion.

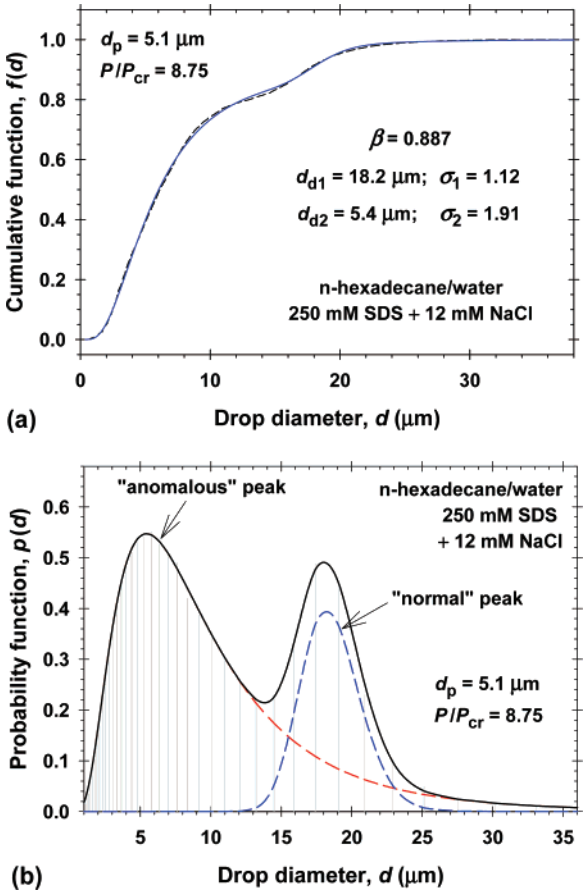

Figure 5. Bimodal size distribution of the drops in an O/W emulsion: $P/P_{cr} = 8.75$; $d_p = 5.1$ μm. (a) Fit of the experimental cumulative function (the dashed line, eq 3.2) with the theoretical cumulative function (the solid line, eq 3.7); the parameters determined from the fit are shown in the figure. (b) Drop size distribution presented by the probability function, $p(d)$, which is calculated from eq 3.6 using the parameter values determined from the fit; $p(d)$ is presented as a superposition of a "normal" (d_{d1}, σ_1) and an "anomalous" (d_{d2}, σ_2) peak. The oil phase is *n*-hexadecane; the water phase contains 250 mM SDS + 12 mM NaCl.

0.01 or 10 mM SDS containing 10 mM added NaCl. The emulsion is generated at a transmembrane pressure, P, which is slightly greater than the critical one, $1 < P/P_{cr} < 2$.

The fits of the experimental cumulative functions with the theoretical ones (Figure 3) yield $d_d = 33.1$ μm and $\sigma = 1.43$ for the solutions with 0.01 mM SDS, and $d_d = 18.8$ μm and $\sigma = 1.10$ for the solutions with 10 mM SDS.

Having determined d_d and σ, with the help of eq 3.3 we calculated the drop-size distribution, $p(d)$. The solid lines in Figure 4a,b represent the $p(d)$ functions corresponding to the two theoretical $f(d)$ functions in Figure 3. The $p(d)$ functions are compared with the respective histograms of the experimental data, which are presented as bar charts. The interval $d_d/\sigma \le d \le d_d\sigma$ that contains 50% of the drops is also shown in the figures. For the lower SDS concentration (0.01 mM SDS, Figure 4a), the dimensionless dispersion, $\sigma = 1.43$, is markedly greater than 1, and, correspondingly, the distribution $p(d)$ is non-symmetric. For the greater SDS concentration (10 mM SDS, Figure 4b), the dimensionless dispersion, $\sigma = 1.1$, is close to 1, and, correspondingly, $p(d)$ is close to a symmetric Gaussian distribution.

Note that our fits of the experimental data have been intentionally carried out in terms of the cumulative function $f(d)$ (Figure 3), rather than in terms of the probability function $p(d)$ (Figure 4). The reason is that the experimental cumulative function ($f(d_k)$ in eq 3.2) is uniquely defined, whereas the choice of the intervals for the histogram bins (Figure 4) could introduce elements of subjectivism.

It should be also noted that the drop-size distribution is unimodal at relatively low applied transmembrane pressures, $1 < P/P_{cr} < 3$. At greater applied pressures ($3 < P/P_{cr} < 11$), the drop-size distribution is bimodal.

(*b) Bimodal Distributions.* Figure 5a shows a typical experimental cumulative function (the dashed line) for the distribution of *n*-hexadecane emulsion droplets at intermediate pressures, $3 < P/P_{cr} < 11$. In this specific experiment, the mean diameter of the membrane pores is $d_p = 5.1$ μm, and the applied transmembrane pressure is $P/P_{cr} = 8.75$; the aqueous phase contains 250 mM SDS and 12 mM NaCl. The experimental cumulative function is fitted by means of eq 3.7. The experimental and theoretical curves (the dashed and solid lines) coincide almost everywhere in Figure 5a. The parameters of the bimodal lognormal distribution (eq 3.6) determined from the best fit are $d_{d1} = 18.2$ μm, $\sigma_1 = 1.12$, $d_{d2} = 5.44$ μm, $\sigma_2 = 1.91$, and $\beta = 0.887$.

With the above parameter values, using eq 3.6, we calculated the respective drop-size distribution, $p(d)$, which is shown in Figure 5b. The two constituent unimodal distributions (the two terms in eq 3.6) are shown in the figure by dashed lines. The peak of the bigger droplets (of mean diameter $d_{d1} = 18.2$ μm) is symmetric and relatively narrow: 50% of the drops are contained within the interval $16.3 \le d < 20.4$ (μm). In contrast, the peak of the smaller drops (of mean diameter $d_{d2} = 5.44$ μm)

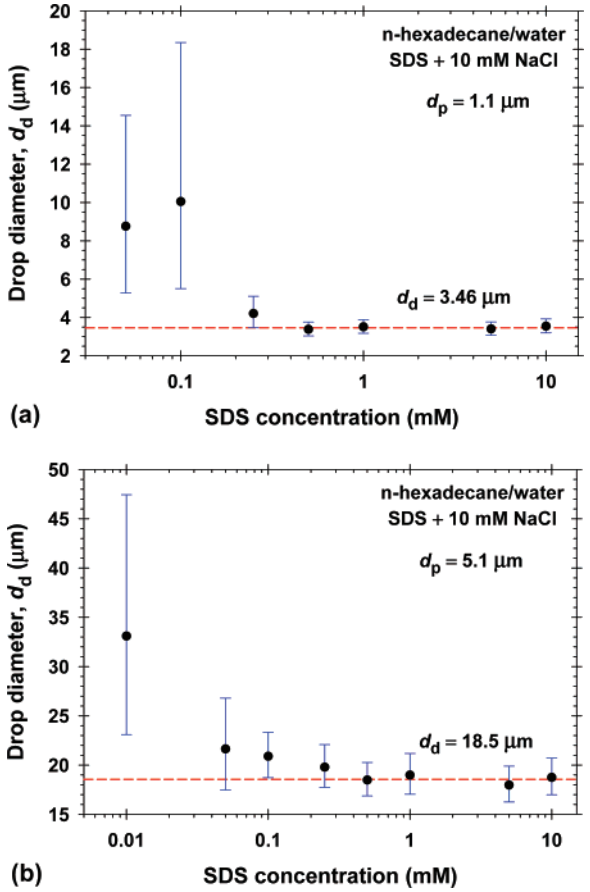

Figure 6. Dependence of the mean diameter, d_d, of *n*-hexadecane emulsion droplets on the concentration of SDS in the presence of 10 mM NaCl. SPG membranes of pore diameters (a) $d_p = 1.1$ μm and (b) $d_p = 5.1$ μm have been used. The error bars correspond to the polydispersity interval of the lognormal distribution: $d_d/\sigma < d < d_d\sigma$.

is asymmetric and relatively broad: 50% of the drops are contained within the interval $2.8 \leq d < 10.4$ (μm).

The approach for data processing described in the present section is further applied to process all data for the drop size, which have been obtained to investigate the effects of surfactant concentration, interfacial tension, the viscosities of the two liquid phases, pore diameter, and applied transmembrane pressure (see below).

4. Influence of Various Factors

4.1. Effect of Surfactant Concentration. To investigate the effect of surfactant concentration, we determined experimentally the mean drop diameter, d_d, as a function of the concentration of SDS at a fixed concentration of NaCl (10 mM) (see Figure 6). The oil phase is *n*-hexadecane. In this series of experiments, the working pressure was $P/P_{cr} \approx 1.1$. Membranes of two different mean pore diameters were used: $d_p = 1.1$ μm (Figure 6a), and $d_p = 5.1$ μm (Figure 6b).

As seen in Figure 6, at the *lower* surfactant concentrations, the drops are bigger and polydisperse. The error bars correspond to the interval $d_d/\sigma \leq d \leq d_d\sigma$ that contains 50% of the drops (see section 3). The asymmetric size distribution shown in Figure 4a (0.01 mM SDS) corresponds to this concentration range.

In contrast, beginning from a certain sufficiently high SDS concentration, which is 0.5 mM in Figure 6a,b, the oil drops are almost monodisperse, their size distribution is symmetric (Figure 4b), and their mean diameter, d_d, is independent of the surfactant concentration.

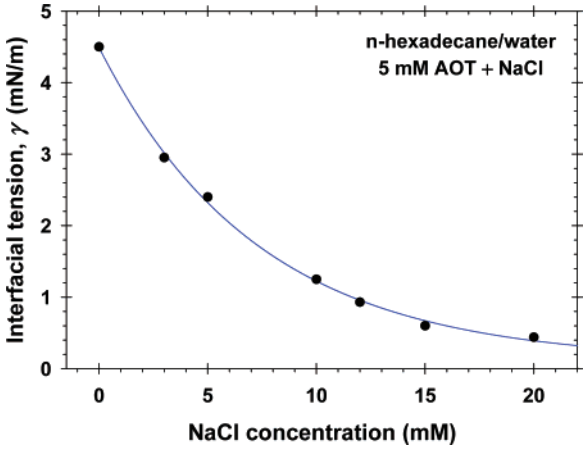

Figure 7. Plot of the interfacial tension of the boundary between *n*-hexadecane and aqueous solutions of 5 mM AOT vs the concentration of NaCl in the water phase. The solid line is a guide to the eye.

The fact that the emulsion drops are larger and polydisperse at the lower surfactant concentrations (Figure 6) can be explained with the coalescence of drops in this case. Different mechanisms of larger drop formation are possible: (i) coalescence in the bulk of the aqueous phase after the detachment of the drops from the membrane; (ii) coalescence of drops during their growth at two neighboring pores of the membrane;[16] (iii) expansion of the contact line on the membrane surface so that one drop is fed by several pores.[3]

As mentioned above, in the specific case of SDS solutions (Figure 6) the "stabilization" of the membrane emulsification process occurs at SDS concentrations greater than or equal to 0.5 mM. The latter concentration is lower than the critical micellization concentration, which is ~4 mM SDS in the presence of 10 mM added NaCl. Fitting the experimental interfacial tension isotherm from ref 24 by means of the van der Waals equation for ionic surfactants,[25,26] we found that the surface coverage (the relative adsorption) is 0.558, and the Gibbs elasticity is 34 mN/m at 0.5 mM SDS + 10 mM NaCl.

The main role of surfactants in membrane emulsification is to stabilize the emulsion drops. So, whatever the mechanism of coalescence could be, in the following we will work at sufficiently high surfactant concentrations that result in stability of the formed drops. In other words, all the data in the rest of this paper correspond to the region of not-too-low concentrations, where the drop diameter, d_d, is independent of the surfactant concentration. In this region, the effect of drop coalescence is suppressed, and each drop grows at the orifice of a single pore.

4.2. Effect of Interfacial Tension. The addition of NaCl considerably reduces the interfacial tension of the AOT solutions. We carried out interfacial tension measurements and membrane emulsification experiments with aqueous solutions containing 5 mM AOT at various NaCl concentrations. The interfacial tension, γ, of these solutions was measured by means of a drop shape analysis system (DSA 10, Krüss GmbH, Hamburg, Germany). One sees (Figure 7) that the decrease in γ is 10-fold, from 4.5 mN/m (without NaCl) down to 0.44 mN/m (in the presence of 20 mM NaCl).

With the same series of AOT solutions, we carried out membrane emulsification experiments at $d_p = 1.1$ μm and P/P_{cr}

(24) Gurkov, T. D.; Todorova, D. T.; Marinova, K. G.; Bilke-Crause, C.; Gerber, C.; Ivanov, I. B. *Colloids Surf., A* **2005**, *261*, 29−38.
(25) Kralchevsky, P. A.; Danov, K. D.; Broze, G.; Mehreteab, A. *Langmuir* **1999**, *15*, 2351−2365.
(26) Kolev, V. L.; Danov, K. D.; Kralchevsky, P. A.; Broze, G.; Mehreteab, A. *Langmuir* **2002**, *18*, 9106−9109.

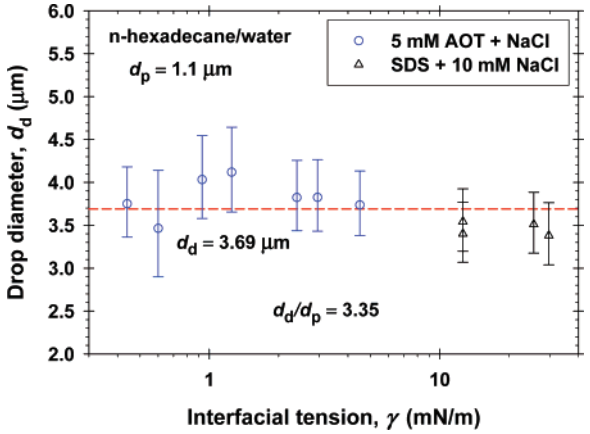

Figure 8. Plot of the mean drop diameter, d_d, vs the interfacial tension, γ, for *n*-hexadecane-in-water emulsions. The mean pore diameter is $d_p = 1.1$ μm. The values of γ are for solutions of 5 mM AOT at various concentrations of NaCl (Figure 7), and for solutions of SDS at 10 mM added NaCl (Figure 6a). The error bars correspond to the polydispersity interval of the lognormal distribution: $d_d/\sigma < d < d_d\sigma$.

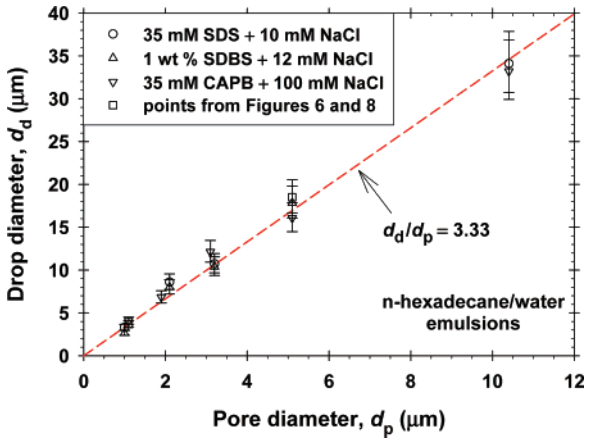

Figure 9. Plot of the mean diameter of *n*-hexadecane emulsion drops, d_d, vs the pore diameter, d_p, for various surfactants in the aqueous phase (35 mM SDS + 10 mM NaCl; 1 wt % SDBS + 12 mM NaCl; 35 mM CAPB + 100 mM NaCl), and experimental points from Figure 6 (SDS + 10 mM NaCl) and Figure 8 (5 mM AOT + NaCl). The error bars correspond to the polydispersity interval of the lognormal distribution: $d_d/\sigma < d < d_d\sigma$.

≈ 1.1; the oil phase was *n*-hexadecane. Under the same conditions (the same d_p, P/P_{cr} and oil phase), we also performed experiments with SDS + 10 mM NaCl. The data for the diameters of the emulsion drops were processed by means of the unimodal lognormal size distribution (see section 3), and the mean drop diameter, d_d, was determined. In Figure 8, the results for d_d are plotted versus γ for the investigated solutions of AOT and SDS. One sees that d_d is insensitive to γ, despite the fact that γ varies by orders of magnitude (from 0.44 to 29.8 mN/m, i.e., 68 times). The mean value of d_d in Figure 8 corresponds to $d_d/d_p \approx 3.35$. We obtained a similar result (d_d/d_p independent of γ) using membranes of different average pore diameters, $1.1 \le d_p \le 10.4$ (μm) (see Figure 9).

4.3. Effect of the Viscosities of the Two Phases. Here, following the notations in ref 15, we denote by η_a the viscosity of the inner (disperse) phase, and by η_b the viscosity of the outer (continuous) phase. Our aim is to compare data for various systems obtained at different values of the ratio η_b/η_a. The data in Figures 9−11 refer to not-too-low surfactant concentrations corresponding to the region of constant d_d in Figure 6. Moreover, the data in

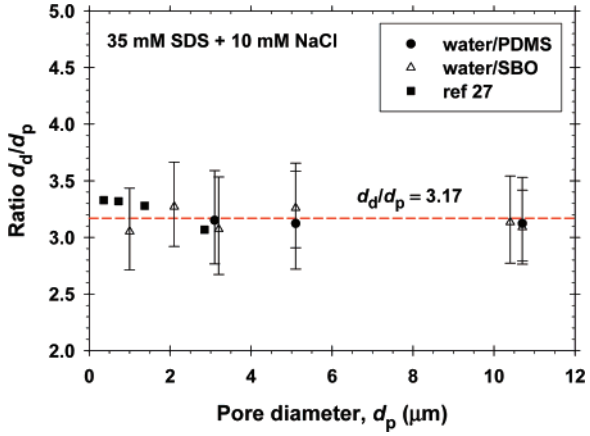

Figure 10. Dependence of the ratio d_d/d_p on the pore diameter, d_p, for two oil phases, PDMS and SBO, of viscosities $\eta_a = 50$ and 500 mPa·s, respectively. The aqueous surfactant solution contains 35 mM SDS and 10 mM NaCl. The experimental results from ref 27 correspond to SBO-in-water emulsions stabilized by lysophosphatidylcholin. The error bars represent the polydispersity interval of the lognormal distribution: $d_d/\sigma < d < d_d\sigma$.

Figures 9−11 are obtained at relatively low transmembrane pressures, $1 < P/P_{cr} < 3$.

In Figure 9, we present our data for *n*-hexadecane-in-water emulsions produced in the presence of four different water-soluble surfactants, SDS, SDBS, CAPB, and AOT, at different concentrations of NaCl in the aqueous phase. SPG membranes of pore diameters in the range $1.1 \le d_p \le 10.4$ (μm) have been used. As seen in the figure, all these diverse systems are characterized by close values of the ratio d_d/d_p, the mean value being $d_d/d_p = 3.33$. For all these systems, the viscosity of the oil (*n*-hexadecane) phase is $\eta_a = 3$ mPa·s, and the viscosity of the water phase is $\eta_b = 0.9$ mPa·s; hence, $\eta_b/\eta_a = 0.3$.

In Figure 10 we present data for d_d/d_p obtained with oils of higher viscosity, that is, at greater η_a, whereas $\eta_b = 0.9$ mPa·s is the same as that in Figure 9. For SBO, we have $\eta_a = 50$ mPa·s and $\eta_b/\eta_a = 1.8 \times 10^{-2}$; for the silicone oil (PDMS) we have $\eta_a = 500$ mPa·s and $\eta_b/\eta_a = 1.8 \times 10^{-3}$. The data in Figure 10 indicate that d_d/d_p is insensitive to the pore diameter, d_p; the mean value is $d_d/d_p = 3.17$. A similar mean value, $d_d/d_p = 3.18$, was obtained in ref 27 for SBO-in-water emulsions (see the square symbols in Figure 10). Values of d_d/d_p of about 3 have also been reported in other membrane-emulsification experiments.[2,3,16,18,19,28,29] Comparison of the values of d_d/d_p in Figures 9 and 10 indicates that the *decrease* in the viscosity ratio, η_b/η_a, by orders of magnitude does not produce a significant effect on the diameter ratio d_d/d_p.

To see how an *increase* in the viscosity ratio, η_b/η_a, would influence the diameter ratio, d_d/d_p, in Figure 11 we show experimental data for emulsions in which the continuous (water) phase contains 62 wt % glycerol. This leads to $\eta_b = 11$ mPa·s, and $\eta_b/\eta_a \approx 3.7$ (the oil phase is *n*-hexadecane). From the slope of the straight line in Figure 11 we calculate $d_d/d_p = 4.26 \pm 0.09$. Hence, for $\eta_b/\eta_a \approx 3.7$, the ratio d_d/d_p is markedly greater than in the cases with $\eta_b/\eta_a \le 1$ (Figures 9 and 10).

In summary, the experiments indicate that, for $\eta_b/\eta_a \le 1$, the diameter ratio, d_d/d_p, is about 3.2 − 3.7, and d_d/d_p is insensitive to the specific value of η_b/η_a. At a higher value of the viscosity ratio ($\eta_b/\eta_a \approx 3.7$), the diameter ratio becomes greater ($d_d/d_p \approx$

(27) Mine, Y.; Shimizu, M.; Nakashima, T. *Colloids Surf., B* **1996**, *6*, 261−268.
(28) Nakashima, T.; Nakamura, K.; Kochi, M.; Iwasaki, Y.; Tomita, M. *Nippon Shokuhin Kogyo Gakkaishi* **1994**, *41*, 70−76.
(29) Joscelyne, S. M.; Trägårdh, G. *J. Food Eng.* **1999**, *39*, 59−64.

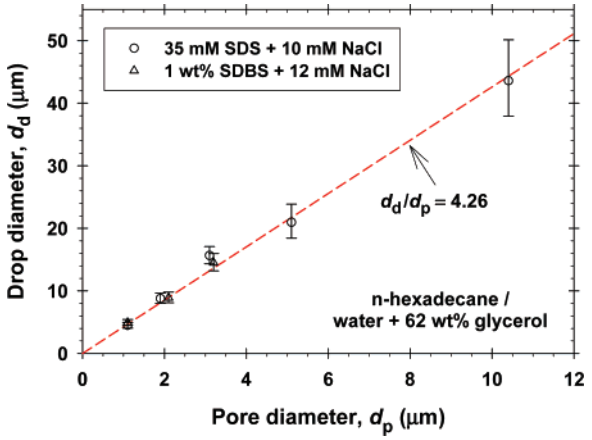

Figure 11. Plot of the mean diameter of O/W emulsion drops, d_d, vs the pore diameter, d_p, for a continuous phase of viscosity, η_b = 11 mPa·s, due to the dissolution of 62 wt % of glycerol in the water, which also contains 35 mM SDS + 10 mM NaCl or 1 wt % SDBS + 12 mM NaCl. The error bars represent the polydispersity interval of the lognormal distribution: $d_d/\sigma < d < d_d\sigma$.

4.3). This effect of the viscosities on the diameter of the produced drops is interpreted in sections 5.4 and 5.5.

4.4. Effect of Pore Diameter. Figures 9−11 also indicate that, at a given viscosity ratio, η_b/η_a, the diameter ratio is practically independent of the pore diameter (i.e., $d_d/d_p \approx$ const). In other words, the diameter of the produced drops, d_d, is proportional to the diameter of the pores, d_p. As mentioned in the beginning of section 4.3, this result is obtained at relatively low applied transmembrane pressures, $1 < P/P_{cr} < 3$. At greater pressures, bimodal drop-size distributions are observed, as shown in Figure 5 and described in the next subsection.

4.5. Effect of Transmembrane Pressure. As illustrated in Figure 5, at $P/P_{cr} > 3$, the drops produced by membrane emulsification could have a bimodal size distribution. To investigate this effect, we carried out systematic experiments with membranes of two different pore diameters: $d_p = 5.1$ and 10.4 μm. In these experiments, the aqueous phase contained 250 mM SDS + 12 mM NaCl, and the oil phase was *n*-hexadecane. (The high SDS concentration guarantees that the coalescence of drops is excluded.) Depending on the shape of the cumulative function, the data for the drop diameters were fitted by unimodal or bimodal lognormal distribution (see section 3).

At the lower transmembrane pressures, $1 < P/P_{cr} < 3$ (region A in Figure 12), we observe only the "normal" unimodal drop-size distribution, whose peak corresponds to $d_d/d_p = 3.2-3.7$.

At greater transmembrane pressures, $3 < P/P_{cr} < 11$ (region B in Figure 12), in addition to the "normal" peak, one observes an "anomalous" peak, with $d_d/d_p = 0.8-2$.

At the greatest investigated transmembrane pressures, $P/P_{cr} > 11$ (region C in Figure 12), the "normal" peak disappears, but the "anomalous" peak remains, and the drop-size distribution becomes unimodal again.

These results are presented in Figure 12, where the most probable drop diameters for the "normal" and "anomalous" peak are denoted by d_{d1} and d_{d2}, respectively, and β denotes the probability for the appearance of the of the "anomalous" peak (see eq 3.6). The parameters d_{d1}, d_{d2}, and β are determined from the best fits of the respective cumulative functions as explained in section 3. As a rule, the "normal" peak is relatively monodisperse and symmetric (σ close to 1), whereas the "anomalous" peak is polydisperse and asymmetric ($\sigma > 1.5$) (see Figure 5b). A possible explanation of the results for the effect of transmembrane pressure on the size of the produced drops (Figure 12) is proposed in sections 5 and 6.

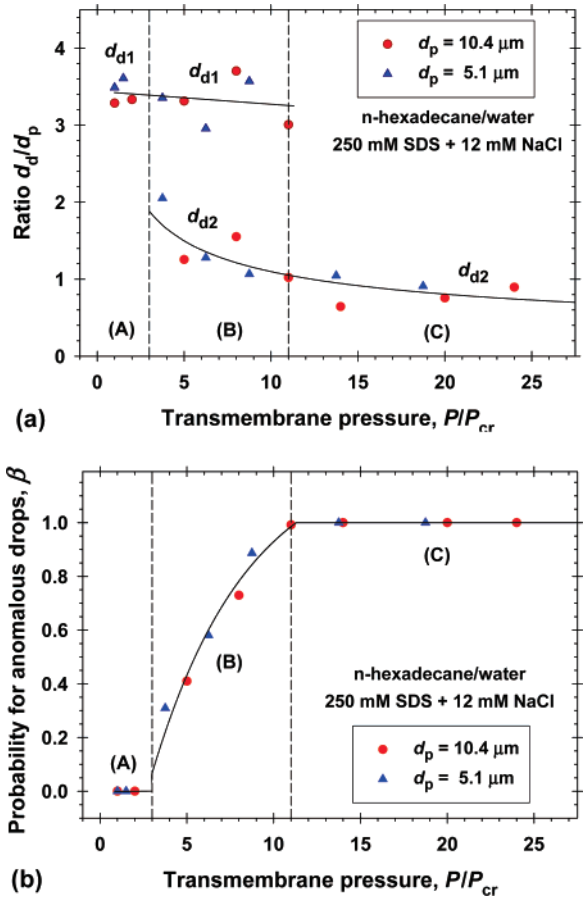

Figure 12. Results from the fits of experimental data for the drop sizes in *n*-hexadecane-in-water emulsions by means of the lognormal distributions in section 3. (a) Plot of d_d/d_p vs P/P_{cr}; the two branches correspond to the "normal" and "anomalous" drops of diameters d_{d1} and d_{d2}, respectively. (b) Plot of β vs P/P_{cr} (see eq 3.6). The water phase contains 250 mM SDS and 12 mM NaCl; membrane pore diameters are $d_p = 5.1$ and 10.4 μm. The solid lines are guides to the eye.

5. Theoretical Modeling of Drop Detachment

Here, our purpose is to develop a theoretical model of drop detachment from the orifice of a pore and to compare the mean drop diameter predicted by the model with the experimental drop-size distributions.

5.1. Analogy with the Detachment of Pendant Drops. It is known that a drop suspended from a tube becomes unstable and detaches when its weight reaches a certain maximum value.[30−36] This fact has been utilized by the maximum drop weight (volume) method for determining the surface tension.[37−41] In other words, there is a maximum body force (gravitational force) exerted on a pendant drop beyond which the drop shape becomes unstable. It has been established that the maximum volume of the pendant

(30) Lohnstein, T. *Ann. Phys.* **1906**, *20*, 237−268.
(31) Lohnstein, T. *Ann. Phys.* **1906**, *21*, 1030−1048.
(32) Lohnstein, T. *Ann. Phys.* **1907**, *22*, 767−781.
(33) Pitts, E. *J. Fluid Mech.* **1974**, *63*, 487−508.
(34) Pitts, E. *J. Inst. Math. Appl.* **1976**, *17*, 387−397.
(35) Michael, D. H.; Williams, P. G. *Proc. R. Soc. London, Ser. A* **1976**, *351*, 117−128.
(36) Michael, D. H. *Annu. Rev. Fluid Mech.* **1981**, *13*, 189−215.
(37) Bashforth, F.; Adams, J. G. *An Attempt to Test the Theories of Capillary Action by Comparing the Theoretical and Measured Forms of Drops of Fluid*; Cambridge University Press: Cambridge, U.K., 1883.
(38) Harkins, W. D.; Brown, F. E. *J. Am. Chem. Soc.* **1919**, *41*, 499−524.
(39) Rusanov, A. I.; Prokhorov, V. A. *Interfacial Tensiometry*; Elsevier: Amsterdam, 1996.
(40) Pu, B.; Chen, D. *J. Colloid Interface Sci.* **2001**, *235*, 265−272.
(41) Pu, B.; Chen, D. *J. Colloid Interface Sci.* **2001**, *235*, 273−277.

drop, V_{max}, which is determined from the solution of Laplace equation of capillarity,[42−44] is approximately equal to the maximum drop volume, which corresponds to the solution of the respective stability problem.[30−36]

In the case of emulsion drops ejected from a capillary, we will use the model assumption that the drop detaches when the hydrodynamic force acting on it becomes equal to the threshold body force that would cause instability of the drop profile and drop detachment.[45] Below, we will first briefly consider the condition for detachment of pendant drops in a gravitational field.

The profile of an axisymmetric pendant drop satisfies the Laplace equation of capillarity, which can be expressed in the form[42−44]

$$\frac{\gamma}{r}\frac{\mathrm{d}}{\mathrm{d}r}(r\sin\varphi) = \frac{2\gamma}{b} - \Delta\rho g z \tag{5.1}$$

Here, r and z are the radial and vertical cylindrical coordinates; the coordinate origin is located at the apex of the drop surface; φ is the running meniscus slope angle, $\tan\varphi = \mathrm{d}z/\mathrm{d}r$; b is the curvature radius at the bottom of the drop; $\Delta\rho$ is the difference between the mass densities of the fluids inside and outside the drop; g is the acceleration due to gravity; and γ is the interfacial tension. The characteristic length-scale of this problem is determined by the capillary length:

$$a = [\gamma/(\Delta\rho g)]^{1/2} \tag{5.2}$$

Introducing dimensionless variables,

$$\tilde{r} = r/a,\ \tilde{z} = z/a,\ \tilde{b} = b/a \tag{5.3}$$

one can bring eq 5.1 into the following dimensionless form:

$$\frac{1}{\tilde{r}}\frac{\mathrm{d}}{\mathrm{d}\tilde{r}}(\tilde{r}\sin\varphi) = \frac{2}{\tilde{b}} - \tilde{z} \tag{5.4}$$

Further, with the help of eq 5.4, the whole stability analysis is carried out in terms of the dimensionless variables. It is convenient to also introduce the dimensionless drop volume and radius of the contact line (of the pore):

$$\tilde{V} = V/a^3,\ \tilde{r}_p = r_p/a \tag{5.5}$$

where $r_p = d_p/2$. Solving eq 5.4 for a series of $\tilde{b}$ values, one could calculate the respective values of $\tilde{V}$ and of the dimensionless height of the pendant drop, $\tilde{h}$. The plot of $\tilde{V}$ versus $\tilde{h}$ exhibits a maximum, $\tilde{V}_{max}$, whose magnitude and position depend on the pore radius, $\tilde{r}_p$. The theoretical analysis and experiments indicate that the drop is stable up to the point of the volume maximum, and becomes unstable at this point.[33−36] Harkins and Brown[38] expressed the maximum gravitational force (weight) for a pendant drop as follows:

$$F_{max}^{(g)} \equiv \Delta\rho g V_{max} = 2\pi r_p \gamma f_d \tag{5.6}$$

where f_d is a correction factor. The original form of eq 5.6 involves the volume of the falling drop, V_f, instead of V_{max}. Because the volume of the residual drop (if any) is usually negligible, here we will work with $V_f \approx V_{max}$. With the help of eqs 5.2 and 5.6, we obtain

$$f_d = \frac{\Delta\rho g}{2\pi r_p \gamma} V_{max} = \frac{1}{2\pi\lambda}(\tilde{V}_{max})^{2/3} \tag{5.7}$$

where the parameters $\tilde{V}_{max}$ and λ are defined as follows:

$$\tilde{V}_{max} \equiv \frac{V_{max}}{a^3},\ \lambda \equiv \frac{r_p}{V_{max}^{1/3}} = \frac{\tilde{r}_p}{\tilde{V}_{max}^{1/3}} \tag{5.8}$$

By integration of the Laplace equation (eq 5.4), for various $\tilde{r}_p$ one can calculate the dependence of $\tilde{V}_{max}$ on λ. The numerical calculations are complex and time-consuming. The obtained results are summarized in tables and interpolation formulas.[38−42] The interpolation formulas used by us are given in Appendix A.

The fact that $\tilde{V}_{max}(\lambda)$ is a universal function, independent of the capillary length, a, is utilized by the *drop volume method*: From the experimental r_p and V_{max}, one determines λ using eq 5.8. Then, from the respective interpolation formula (or tables) for $\tilde{V}_{max}(\lambda)$ [or $f_d(\lambda)$; see eq 5.7], one calculates $\tilde{V}_{max}$. Further, one determines $a = (V_{max}/\tilde{V}_{max})^{1/3}$, and finally, from a one obtains γ using the definition of the capillary length (eq 5.2; see, e.g., refs 40 and 41).

5.2. Condition for Drop Detachment from the Orifice of a Pore. Coming back to the case of membrane emulsification, we have to note that the emulsion droplets are so small that the gravitational deformation of their surfaces is completely negligible. However, the emulsion droplets, growing at the opening of a membrane pore, can be deformed by the hydrodynamic ejection force that is due to the inner liquid, which flows along the pores and inflates the droplets. The hydrodynamic ejection force can also induce elongation of the drop profile, like the gravitational force in the case of a pendant drop. An elongated drop has a limit of its stability (maximum volume), after which it becomes unstable and detaches from the pore. Here, we will make the model assumption that, at the moment of detachment, the hydrodynamic ejection force, F_h, acting on the drop is equal to the critical capillary force that corresponds to the stability−instability transition in the drop profile:[45]

$$F_h = 2\pi r_p \gamma f_d \tag{5.9}$$

(see also eq 5.6). As mentioned above, the Harkins−Brown factor f_d is independent of the capillary length, a, and the gravity acceleration, g. The hydrodynamic ejection force, acting on the forming emulsion drop, can be expressed in the following form:[15]

$$F_h = \eta_a r_p v_m f_h \tag{5.10}$$

$$f_h(\alpha) \equiv f_{a,0}(\alpha) + \frac{\eta_b}{\eta_a}[f_b(\alpha) + f_{ab}(\alpha)] \tag{5.11}$$

where v_m is the mean velocity of the flow of the inner liquid in a pore of the membrane, and f_h is the hydrodynamic force coefficient; the angle α characterizes the size of the drop protruding from the membrane: $\sin\alpha = r_p/r_s$ (Figure 13). The force coefficient f_h in eq 5.11 is a superposition of three different contributions:[15] (i) from the inner (disperse) phase, $f_{a,0}(\alpha)$, (ii) from the outer (continuous) phase, $f_b(\alpha)$, and (iii) from the interplay of the hydrodynamic flows in the two phases at the boundary between them (at the drop surface), $f_{ab}(\alpha)$. The hydrodynamic problem is solved in ref 15 for the case of low Reynolds numbers, and tangentially immobile drop interface,

(42) Hartland, S.; Hartley, R. W. *Axisymmetric Fluid−Liquid Interfaces*; Elsevier: Amsterdam, 1976.
(43) Finn, R. *Equilibrium Capillary Surfaces*; Springer-Verlag: New York, 1986.
(44) Kralchevsky, P. A.; Nagayama, K. *Particles at Fluid Interfaces and Membranes*; Elsevier: Amsterdam, 2001; Chapter 2.
(45) Hartland, S.; Kumar, A. *Colloids Surf., A* **1994**, *83*, 245−254.

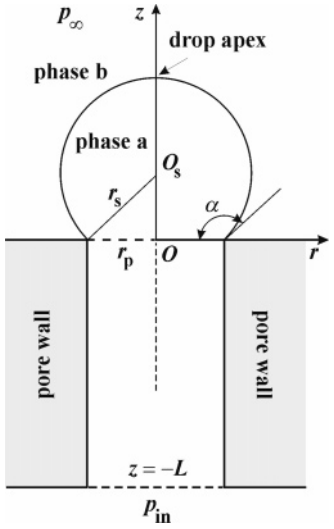

Figure 13. Sketch of a drop protruding from a cylindrical pore of radius r_p. The oil−water interface is spherical, of radius r_s. At a given r_p, the "protrusion" angle α characterizes the size of the drop ($0 < \alpha < 180°$; $\sin\alpha = r_p/r_s$). The *z*-axis is directed along the axis of the pore; the plane $z = 0$ corresponds to the orifice of the pore; p_{in} is the pressure in the inner phase "a" at the level $z = -L$; p_∞ is the pressure in the bulk of the outer phase "b".

which has a spherical shape of radius r_s. The expressions for calculating the coefficients $f_{a,0}(\alpha)$, $f_b(\alpha)$, and $f_{ab}(\alpha)$ are given in Appendix A. All of them are universal functions of the protrusion angle, α.

Substituting eqs 5.7 and 5.10 into eq 5.9, we obtain the following *condition (criterion) for drop detachment*:

$$f_h v_m = \frac{\gamma}{\lambda \eta_a}[\tilde{V}_{max}(\lambda)]^{2/3} \tag{5.12}$$

where $\tilde{V}_{max}(\lambda)$ is a universal function that can be calculated as explained in Appendix A. Substituting an appropriate expression for the mean velocity, v_m, in eq 5.12, we obtain an equation for determining λ. With the obtained value of λ, we can further find the diameter of the detached drop, d_d:

$$\frac{d_d}{d_p} = \frac{r_d}{r_p} = \frac{1}{r_p}\left(\frac{3V_{max}}{4\pi}\right)^{1/3} = \left(\frac{3}{4\pi}\right)^{1/3}\frac{1}{\lambda} \approx \frac{0.62035}{\lambda} \tag{5.13}$$

We have used eq 5.8 and the fact that the volume of the detached drop is $V_{max} = (4/3)\pi r_d^3$. In the case of a spherical oil−water interface, the volume of the drop protruding from the pore is (Figure 13)

$$V = \frac{\pi r_p^3}{3}\frac{2 + \cos\alpha}{(1 + \cos\alpha)^2}\sin\alpha \tag{5.14}$$

Setting $V = V_{max}$ in eq 5.14, and using eq 5.8, we derive a relationship between λ and α:

$$\frac{1}{\lambda^3} = \frac{\pi}{3}\frac{2 + \cos\alpha}{(1 + \cos\alpha)^2}\sin\alpha \tag{5.15}$$

The value of α in eq 5.15 refers to the moment of drop detachment. Below, we consider two important special cases, corresponding to regimes of drop formation (i) at constant flow rate and (ii) at constant transmembrane pressure.

5.3. Regime of Constant Flow Rate. Experimentally, this regime could be realized when the disperse phase is supplied by a motorized syringe in a separate capillary channel. The flow rate can be expressed in the form

$$Q = \frac{V_{max}}{t_d} \tag{5.16}$$

where t_d is the period of drop detachment from the orifice of the channel. The mean velocity of the liquid is

$$v_m = \frac{Q}{\pi r_p^2} = \frac{V_{max}}{\pi r_p^2 t_d} = \frac{r_p}{\pi \lambda^3 t_d} \tag{5.17}$$

Here, we used eqs 5.16 and 5.8. Substituting eq 5.17 into the condition for drop detachment (eq 5.12), one obtains

$$q \equiv \frac{\eta_a r_p}{\gamma t_d} = \frac{\pi\lambda^2}{f_h(\alpha)}[\tilde{V}_{max}(\lambda)]^{2/3} \tag{5.18}$$

where *q* could be interpreted as a dimensionless flow rate.

To determine the dependence of d_d/d_p on *q*, it is convenient to use the protrusion angle α as a parameter. The computational procedure is the following. First, for a given value of α, we determine λ from eq 5.15. Second, for these values of λ and α, using the expressions in Appendix A, we calculate $\tilde{V}_{max}(\lambda)$ and $f_h(\alpha)$, the latter at a given value of the viscosity ratio η_b/η_a. Finally, from eqs 5.13 and 5.18, we determine r_d/r_p and *q*.

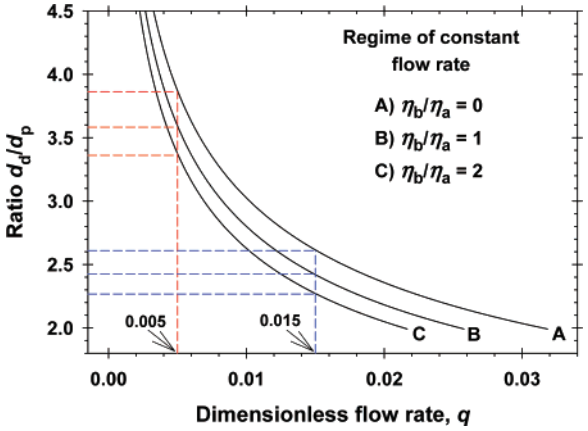

Figure 14. Regime of constant flow rate: dependence of the ratio d_d/d_p on the dimensionless flow rate *q* (see eq 5.18), for three different values of the viscosity ratio, η_b/η_a.

Figure 14 shows the dependence of the drop diameter d_d (scaled with the pore diameter, d_p), on the dimensionless flow rate, *q*, at different values of the viscosity ratio, η_b/η_a. In general, the drop diameter decreases with the increase of *q* and η_b/η_a. The effect of η_b/η_a is not so strong because, in eq 5.11, the viscosity ratio is multiplied by the term $(f_b + f_{ab})$, which is considerably smaller than $f_{a,0}$.

Figure 14 indicates that all factors that increase the dimensionless flow rate, $q = \eta_a r_p/(\gamma t_d)$, lead to a decrease in the ratio d_d/d_p for the produced drops. The dashed lines in this figure show that a 3-fold increase in *q* decreases the sizes of the detached droplets by a factor of about 1.5. The increase in the viscosity of the inner phase η_a (at fixed all other parameters) leads to a greater *q*, and, in view of Figure 14, this should lead to the production of smaller drops in the regime of constant flow rate. Note, however, that our experiments are carried out in the regime of constant transmembrane pressure, for which the increase in the viscosity of the inner phase η_a has a very small, almost negligible effect (compare the values of d_d/d_p in Figures 9 and 10); more details are discussed in the next subsection.

5.4. Regime of Constant Transmembrane Pressure. In membrane emulsification, a constant pressure difference, P, is applied across the microporous membrane, usually, by connecting the experimental setup to a gas bottle (Figure 2).

Let us consider a drop that is growing at the orifice of a cylindrical pore of radius r_p and length L (Figure 13). The pressures in the inner and outer phases (denoted by subscripts "a" and "b", respectively) can be presented in the form[15]

$$p_a \equiv p_\infty + \frac{2\gamma}{r_s} + p_{a,dyn},\ p_b \equiv p_\infty + p_{b,dyn} \tag{5.19}$$

Here, p_∞ is the pressure in the bulk of the outer phase "b", $2\gamma/r_s$ is the capillary pressure of the oil−water interface, and $p_{a,dyn}$ and $p_{b,dyn}$ are the dynamic (viscous) contributions to the scalar pressure in the respective phases. In general, p_a, p_b, $p_{a,dyn}$, and $p_{b,dyn}$ are functions of the position vector, $\mathbf{r}$, and of the protrusion angle, α. The force balance (per unit area) at the apex of the drop surface, that is, at the point where the z-axis pierces the oil−water interface (Figure 13), is[15]

$$\frac{2\gamma}{r_s} + \left(p_b - 2\eta_b \frac{\partial w_b}{\partial z}\right)_{ap} = \left(p_a - 2\eta_a \frac{\partial w_a}{\partial z}\right)_{ap} \tag{5.20}$$

where the subscript "ap" means that the expression in the parentheses should be estimated at the apex of the drop surface; w_a and w_b are the vertical components of the fluid velocity in the phases "a" and "b", and the terms with the derivatives of w_a and w_b represent the contributions from the normal components of the viscous stress tensor to the total stress. Substituting p_a and p_b from eq 5.19 into eq 5.20, we obtain

$$\left(p_{a,dyn} - 2\eta_a \frac{\partial w_a}{\partial z}\right)_{ap} = \frac{\eta_b v_m}{r_p}\frac{f_{ab}}{\pi} \tag{5.21}$$

where[15]

$$f_{ab} = \frac{r_p \pi}{\eta_b v_m}\left(p_{b,dyn} - 2\eta_b \frac{\partial w_b}{\partial z}\right)_{ap} \tag{5.22}$$

f_{ab} can be calculated as explained in Appendix A. It is convenient to work in terms of the dimensionless pressure $\tilde{p}_{a,0}(\mathbf{r})$, which is defined as follows:[15]

$$p_a(\mathbf{r}) = \frac{\eta_a v_m}{r_p}\tilde{p}_{a,0}(\mathbf{r}) + \left(p_a - 2\eta_a \frac{\partial w_a}{\partial z}\right)_{ap} \tag{5.23}$$

The last term in the parentheses is independent of $\mathbf{r}$. In the special case when $\mathbf{r} = (0, 0, -L)$, eq 5.23 reduces to

$$p_{in} = \frac{\eta_a v_m}{r_p}\pi_0(L/r_p) + \left(p_a - 2\eta_a \frac{\partial w_a}{\partial z}\right)_{ap} \tag{5.24}$$

Here, p_{in} is the value of the pressure p_a at level $z = -L$ in the cylindrical channel (Figure 13); π_0 denotes the value of the dimensionless pressure $\tilde{p}_{a,0}(\mathbf{r})$ at $\mathbf{r} = (0, 0, -L)$; π_0 depends on the ratio L/r_p (see eq 5.29 below). Further, substituting p_a from eq 5.19 in the right-hand side of eq 5.24, we obtain

$$p_{in} = \frac{\eta_a v_m}{r_p}\pi_0(L/r_p) + \left(p_{a,dyn} - 2\eta_a \frac{\partial w_a}{\partial z}\right)_{ap} + p_\infty + \frac{2\gamma}{r_s} \tag{5.25}$$

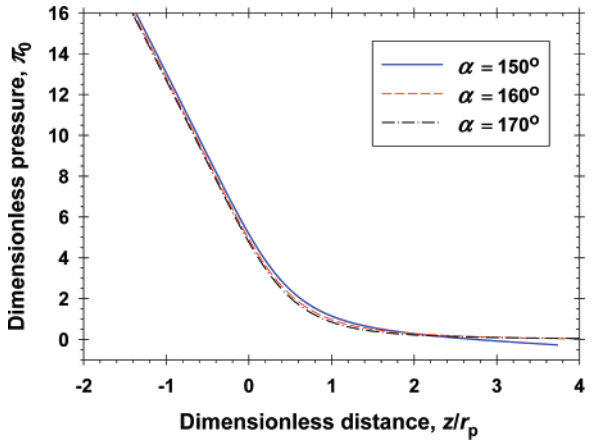

Figure 15. Dependence of the dimensionless pressure π_0 on the dimensionless distance from the orifice of the pore, z/r_p, calculated for three values of the protrusion angle, α, as explained in Appendix B.

With the help of eq 5.21 and the geometrical relationship $r_p/r_s = \sin\alpha$ (Figure 13), we bring eq 5.25 in the form

$$\frac{r_p P_L}{2\gamma} = \frac{\eta_a v_m}{2\gamma}\left[\pi_0(L/r_p) + \frac{\eta_b}{\eta_a}\frac{f_{ab}}{\pi}\right] + \sin\alpha \tag{5.26}$$

where

$$P_L \equiv p_{in} - p_\infty \tag{5.27}$$

is the difference between the pressure at level $z = -L$ in the cylindrical pore and the pressure in the bulk of phase "b" (Figure 13). Finally, we substitute v_m from eq 5.26 into the condition for drop detachment (eq 5.12), which acquires the form

$$\Pi \equiv \frac{r_p P_L}{2\gamma} = \frac{[\tilde{V}_{max}(\lambda)]^{2/3}}{2\lambda f_h(\alpha)}\left[\pi_0(L/r_p) + \frac{\eta_b f_{ab}(\alpha)}{\eta_a \pi}\right] + \sin\alpha \tag{5.28}$$

Here, Π is a dimensionless pressure (P_L scaled by the capillary pressure $2\gamma/r_p$). Plots of π_0 versus z/r_p, calculated as explained in Appendix B, are shown in Figure 15 for $\alpha = 150°$, 160°, and 170°. (From the experimental drop and pore diameters, one can estimate that the drop detachment usually happens at $150° < \alpha < 170°$.) One sees that π_0 is insensitive to α. Substituting $z = -L$, we interpolated the dependence in Figure 15 and obtained the following formula for calculating $\pi_0(L)$:

$$\pi_0(L/r_p) = 8\frac{L}{r_p} + 4.863\left[0.1197 - 1.2999\frac{L}{r_p} + 0.6810\left(\frac{L}{r_p}\right)^2 - 0.0497\left(\frac{L}{r_p}\right)^3\right]\exp\left(-4\frac{L}{r_p}\right) \tag{5.29}$$

where $L/r_p \geq 0$ and $150° \leq \alpha \leq 180°$. The first term in the right-hand side of eq 5.29 corresponds to Poiseuille flow in the channel, whereas the other terms represent small corrections due to edge effects in the vicinity of the channel orifice.

For a given L/r_p, from eq 5.29 one can determine π_0, and then from eq 5.28 one can calculate the dependence of Π on the diameter ratio, d_d/d_p. The computational procedure is the following: The angle α is used as a parameter. For a given α, one calculates λ from eq 5.15. Next, $f_{ab}(\alpha)$, $f_h(\alpha)$, and $\tilde{V}_{max}(\lambda)$ are calculated as explained in Appendix A. Finally, the values of d_d/d_p and Π are obtained from eqs 5.13 and 5.28.

Dependences of Π on d_d/d_p, calculated for three experimental values of the viscosity ratio η_b/η_a (Table 1), are shown in Figure

Table 1. Parameters of the Curves in Figure 16

η_b/η_a	$(d_d/d_p)_{cr}$*	Π_{cr}*	$\alpha(^\circ)$*	π_0	L/r_p
≈0	3.17	1.88	161.6	8.40	0.45
0.3	3.33	1.81	162.6	8.58	0.47
3.67	4.26	1.18	166.4	8.66	0.48

* This value corresponds to the minimum of the respective curve in Figure 16.

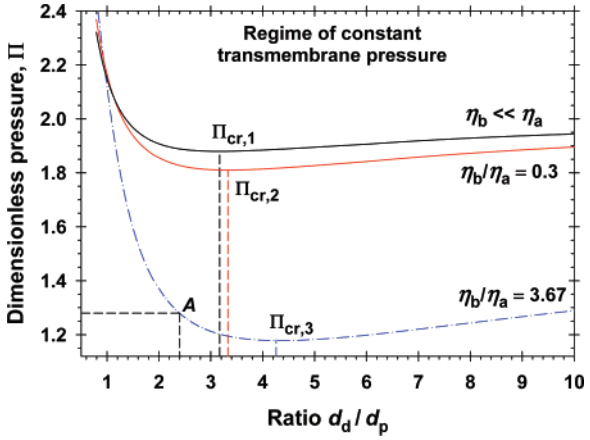

Figure 16. Dependence of the dimensionless pressure Π on d_d/d_p. The three curves are calculated from eq 5.28 for three fixed experimental values of the viscosity ratio, η_b/η_a (Table 1). The minimum of each curve, $\Pi_{cr,j}$ ($j = 1,2,3$), corresponds to the critical pressure for drop detachment. For $\Pi < \Pi_{cr}$, drops cannot be released from the pores. For a given $\Pi > \Pi_{cr}$, the intersection point, *A*, of the respective horizontal line with the calculated curve determines the dimensionless diameter of the formed drops, d_d/d_p.

16. One sees that, at a certain value of the diameters ratio, $(d_d/d_p)_{cr}$, the dimensionless pressure has a minimum corresponding to $\Pi = \Pi_{cr}$. The physical picture ensuing from the curves in Figure 16 is the following:

For pressures smaller than the critical one ($\Pi < \Pi_{cr}$), drops cannot be released from the pores. At $\Pi = \Pi_{cr}$, the first drops are released with size corresponding to $(d_d/d_p)_{cr}$. At a higher pressure, corresponding to point *A* in Figure 16, the size of the detached drops can be determined by projecting the point *A* on the horizontal axis.

In our experiments, the drops (with $d_d = d_{d1}$, Figure 12a) are produced at a pressure that is just above the critical pressure for drop detachment. For this reason, we could identify the experimentally determined diameter ratio (section 4.3 and Table 1) with $(d_d/d_p)_{cr}$, that is, with the position of the minimum of the respective dependence in Figure 16. The derivative of the right-hand side of eq 5.28 was set equal to zero (condition for the minimum), and the value of L/r_p was determined from the obtained equation using the experimental d_d/d_p. The calculated values of L/r_p are close to 0.5 (see the last column of Table 1). This result calls for discussion.

5.5. Discussion. A porous medium (e.g., an SPG membrane) could be modeled both theoretically and experimentally as a system of channels (pores) and chambers (cavities)[46,47] (see Figure 17). The values of *L* in the last column of Table 1, which are on the order of r_p, indicate that *L* could be identified with the length of a channel (Figure 17). (If *L* were the total thickness of the microporous membrane, which is ≈1 mm, we would have $L \gg r_p$, which is not the case.) The fact that the three values of L/r_p in Table 1 (obtained at different η_b/η_a and d_p) are close to each other could be interpreted as an indication that $L/r_p \approx 0.47$ is a structural characteristic of the SPG membranes.

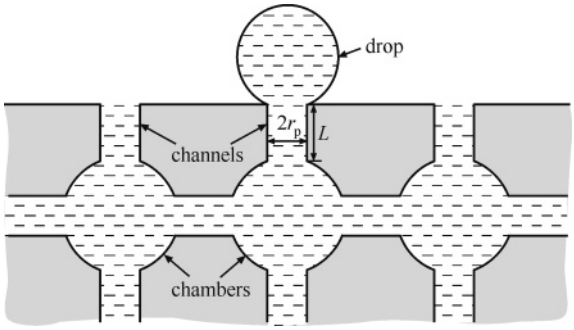

Figure 17. Sketch of a microporous membrane that consists of interconnected channels (pores) and chambers (cavities). Drops are formed at the orifices of the terminal channels (of length *L* and radius r_p) whose openings are at the membrane surface.

Experimentally, when the transmembrane pressure reaches its critical value, one observes the release of drops from isolated "active" pores that are separated at comparatively large distances from each other. With the further increase of the transmembrane pressure, one observes the "activation" of more pores without a noticeable increase in the frequency of drop release from a given pore. These observations are related to the polydispersity of the pores: one can expect that the larger pores are the first that begin to release drops, whereas the smaller pores can be "activated" at greater pressures.

At the critical pressure, at which only some isolated pores are active, the liquid is supplied to an active pore though a large number of channels in the interior of the membrane. Then, the flow rate in these channels will be relatively low, whereas the flow rate in the terminal channel (that feeds the growing droplet, Figure 17) will be much greater. Consequently, the critical pressure difference for the terminal channel, $P_{L,cr}$, should be approximately equal to (slightly smaller than) the experimental critical transmembrane pressure, P_{cr}.

The experimental results are in agreement with this picture. For example, in the case of *n*-hexadecane-in-water emulsions (Figure 12), for which the aqueous phase is a solution of 250 mM SDS + 12 mM NaCl, the interfacial tension is $\gamma = 5$ mN/m, and the viscosity ratio is $\eta_b/\eta_a = 0.3$; for pore diameter $d_p = 10.4$ μm, the *experimental* critical transmembrane pressure is

$$P_{cr} = 3920 \text{ Pa} \tag{5.30}$$

For the minimum of the curve with $\eta_b/\eta_a = 0.3$ in Figure 16, we have $\Pi_{cr} = 1.81$ (see also Table 1). Then, in view of eq 5.28, we obtain the *theoretical* critical pressure difference for the terminal channel (of length *L*):

$$P_{L,cr} \equiv \frac{4\gamma}{d_p}\Pi_{cr} = 3481 \text{ Pa} \tag{5.31}$$

The difference, $P_{cr} - P_{L,cr} = 439$ Pa, can be interpreted as the pressure difference due to the flow through the channels in the interior of the membrane (see above). Similar results have been obtained under other experimental conditions. For example, for pore diameter $d_p = 5.1$ μm (all other parameters being the same), we measured $P_{cr} = 7840$ Pa, whereas the calculations give $P_{L,cr} = 7098$ Pa. Then, the pressure difference due to the channels in the membrane interior is $P_{cr} - P_{L,cr} = 742$ Pa.

As mentioned above, when the total transmembrane pressure *P* is increased, the number of active pores is also increased,

(46) McKellar, M.; Wardlaw, N. C. *J. Can. Pet. Technol.* **1982**, *21*, 39−41.
(47) Vizika, O.; Payatakes, A. C. *Physicochem. Hydrodyn.* **1989**, *11*, 187−204.

whereas the flow rate (and the pressure difference P_L) for each separate active pore remains almost the same. Thus, we could have $P \gg P_L \approx P_{L,cr}$. In this regime, despite the increase in P, the pressure difference for a pore, P_L, is always close to $P_{L,cr}$, that is, close to the minimum of the respective curve in Figure 16. Hence, the size of the released drops is insensitive to the magnitude of the applied pressure, P. This regime gives a possible explanation of the upper branch in Figure 12a (drops of diameter d_{d1}), which corresponds to the "normal" peak (Figure 5b). The slight tendency of d_{d1} to decrease with the rise of P (Figure 12a) could be attributed to a small increase of P_L above $P_{L,cr}$ (see Figure 16). In conclusion, the mean drop diameter for the "normal" peak (that with $d_d = d_{d1}$) corresponds to the quantity $(d_d/d_p)_{cr}$ that represents the position of the minimum of the respective curve in Figure 16.

It is remarkable that, in view of eq 5.28, the position of the minimum, $(d_d/d_p)_{cr}$, is independent of the interfacial tension, γ. In fact, γ is present in the right-hand sides of eqs 5.12 and 5.26, but γ cancels when the latter two equations are combined to derive eq 5.28. The circumstance that $(d_d/d_p)_{cr}$ predicted by eq 5.28 is independent of γ is in agreement with the experimental results in Figure 8.

Likewise, the viscosity of the disperse phase, η_a, is present as a multiplier in the right-hand sides of eqs 5.12 and 5.26, but η_a cancels when the latter two equations are combined to derive eq 5.28. The value of $(d_d/d_p)_{cr}$ predicted by eq 5.28 depends on η_a only through the relatively small term $(\eta_b/\eta_a)f_{ab}$. The latter fact is in agreement with the experimental result (Figures 9 and 10) that the increase of the magnitude of η_a by several orders of magnitude has a rather small effect on the ratio d_d/d_p (see also the positions of the minima for the upper two curves in Figure 16).

In summary, the prediction of the drop diameter, d_d, based on the minimum of the curves in Figure 16 is in agreement with the experimental observations. One has to initially characterize a given type of membrane with the respective value of L/r_p determined for a specific system, as explained above (see Table 1, where $L/r_p \approx 0.47$ was obtained for SPG membranes). Then, eq 5.28 enables one to predict the drop sizes in any other emulsions produced by the membranes of this type.

6. Possible Explanation of the Anomalous Peak

The comparison of theory and experiment (sections 5.4 and 5.5) indicates that the curves with the minima in Figure 16 could give a possible explanation of the "normal" peak in Figure 5b, which corresponds to the upper branch ($d_d = d_{d1}$) in Figure 12a. To find a possible explanation of the "anomalous" peak in Figure 5b that corresponds to the lower branch ($d_d = d_{d2}$) in Figure 12a, we carried out additional experiments, which are described below.

We formed drops at the tip of a glass capillary of inner diameter $d_p = 180$ μm. The outer phase was an aqueous solution of 100 mM SDS + 100 mM NaCl. The inner phase was silicone oil (PDMS) of viscosity 5 mPa·s. The difference between the mass densities of the water and oil phases is 0.08 g/cm^3, so that the instabilities in this system are due mostly to capillary and hydrodynamic (rather than gravitational) effects. The oil was supplied with a constant flow rate by means of a motorized syringe. The only motion in the continuous phase is due to the breakup of oil drops from the capillary (there is no crossflow or other external flow in the continuous phase).

Figure 18a shows three consecutive video frames of the process of drop detachment at a $Q = 10$ mL/min flow rate of oil. The drop breakup happens close to the capillary tip, after the formation of a comparatively short neck. The detached drops are monodisperse, without formation of secondary smaller drops.

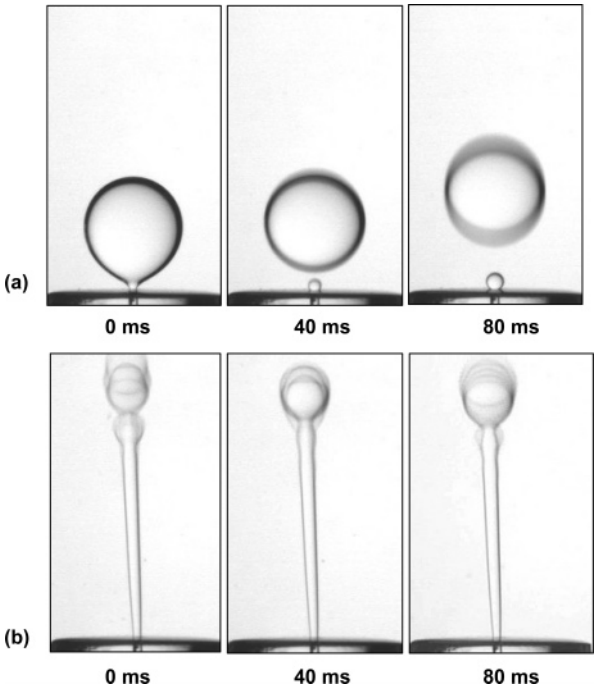

Figure 18. Consecutive frames from a video record of the detachment of oil drops in water from the tip of a capillary of inner diameter $2r_p = 180$ μm. The time is denoted below each frame. (a) At flow rate 10 mL/min, the breakup of drops happens at the capillary tip (dripping mode). (b) At flow rate 270 mL/min, the formation and breakup of drops occurs at the end of an oily filament (jetting mode). The disperse phase is silicone oil (PDMS) of viscosity 5 mPa·s. The continuous phase is an aqueous solution of 100 mM SDS + 100 mM NaCl.

Figure 18b shows three consecutive video frames of the process of drop detachment at a $Q = 270$ mL/min flow rate of oil. In this case, an extended liquid filament (jet) is formed, which ends with a spherical oil drop. This drop is growing until it reaches a certain critical size, and then it breaks up as a result of capillary instability. Experimentally, the diameter of the drops that are formed in this way (Figure 18b) is about 2.6 times smaller than the diameter of the drops formed at the capillary tip (Figure 18a).

These two different mechanisms have been investigated in a number of studies,[48−53] and have been called "dripping" and "jetting" modes of drop breakup. The transition between the two mechanisms occurs at a certain critical flow rate.[48−53] From this viewpoint, the following explanation could be given to the two branches of drops with different diameters in Figure 12a.

The upper branch with $d_d = d_{d1}$ in Figure 12a (the normal peak in Figure 5b), can be identified with drop breakup in *dripping* mode. This interpretation is in agreement with our analysis in sections 5.4 and 5.5. The lower branch with $d_d = d_{d2}$ in Figure 12a (the anomalous peak in Figure 5b), could be explained with

(48) Clanet, C.; Lasheras, J. C. *J. Fluid Mech.* **1999**, *383*, 307−326.
(49) Cramer, C.; Beruter, B.; Fischer, P.; Windhab, E. J. *Chem. Eng. Technol.* **2002**, *25*, 499−506.
(50) Cramer, C.; Fischer, P.; Windhab, E. J. *Chem. Eng. Sci.* **2004**, *59*, 3045−3058.
(51) Cramer, C. Continuous drop formation at a capillary tip and drop deformation in a flow channel. Ph.D. Thesis, Swiss Federal Institute of Technology (ETH), Zurich, 2004.
(52) Ambravaneswaran, B.; Subramani, H. J.; Phillips, S. D.; Basaran, O. A. *Phys. Rev. Lett.* **2004**, *93*, 034501.
(53) Utada, A. S.; Fernandez-Nieves, A.; Stone, H. A.; Weitz, D. A. *Phys. Rev. Lett.* **2007**, *99*, 094502.

drop breakup in *jetting* mode. Indeed, the latter regime is observed at higher transmembrane pressures (and flow rates). The existence of a region of pressures with bimodal drop distribution (overlap of the "normal" and "anomalous" peaks) is probably due to the polydispersity of the membrane pores. Indeed, in the case of Figure 12, one could assume that, for the widest pores, the dripping/jetting transition occurs at $P/P_{cr} \approx 3$, whereas, for the narrowest pores, this transition occurs at $P/P_{cr} \approx 11$. At intermediate pressures, $3 < P/P_{cr} < 11$, the wider pores "work" in the jetting regime, whereas the narrower pores operate in the dripping regime. The relatively wide range of pressures at which bimodal distribution is observed ($3 < P/P_{cr} < 11$) could be explained with the fact that the increase of transmembrane pressure leads not only to an increase in the flow rate through the separate pores, but mostly to activation of additional pores. As mentioned above, the theoretical analysis of the data in section 5 refers to drop breakup in dripping mode, which corresponds to the "normal" peak. Similar analysis for the jetting regime in membrane emulsification could be a subject for a subsequent study.

The most important application of membrane emulsification is for production of emulsions with *monodisperse* drops. For preparation of polydisperse emulsions, one could use other methods such as colloid mills, rotor-stator, and narrow gap homogenizers, which are more productive than the membrane emulsification. The anomalous peak (supposedly due to drop breakup in the jetting regime) has a relatively large polydispersity (Figure 5b). Hence, to produce monodisperse emulsion by membrane emulsification, it is recommendable to work at relatively low transmembrane pressures ($1 < P/P_{cr} < 3$ in Figure 12) in order to obtain drops of normal unimodal distribution that corresponds to drop breakup in dripping mode. As discussed in section 5.5, the mean diameter of such drops is determined by the position of the minimum of the plot of Π versus d_d/d_p (Figure 16) at the respective value of the viscosity ratio η_b/η_a.

7. Summary and Conclusions

Here, we investigate experimentally and theoretically the factors that determine the size of the emulsion droplets produced by membrane emulsification in the "batch regime" (without applied crossflow). Hydrophilic glass membranes of pore diameters between 1 and 10 μm have been used to obtain O/W emulsions. If the surfactant concentration is high enough (>0.5 mM for SDS), the surfactant stabilizes the drops against coalescence, and then their size becomes insensitive to further increase of surfactant concentration and to the type of surfactant used (Figures 6, 8, and 9). This was established in experiments with four emulsifiers: anionic SDS, SDBS, and AOT, and zwitterionic CAPB. All further experiments were carried out at sufficiently high surfactant concentrations that result in stability of the formed drops.

Although, in principle, one could expect that the oil−water interfacial tension, γ, could influence the drop breakup, we experimentally established that the size of the formed drops does not depend on γ (Figure 8). Moreover, the size of the formed drops is insensitive to the increase in the viscosity of the inner (oil) phase, η_a (see Figures 9 and 10). However, the produced drops become markedly bigger when the viscosity of the outer (water) phase, η_b, is increased (compare Figures 9 and 11). The drops are relatively monodisperse when the working transmembrane pressure is slightly above the critical pressure for drop detachment. At higher applied pressures, the drop-size distribution becomes bimodal: superposition of a "normal" peak of monodisperse drops and an "anomalous" peak of polydisperse drops is observed (Figures 5b and 12).

To interpret the experimental results, in section 5 we developed a quantitative theoretical model of drop detachment. Following an analogy with the breakup of pendant drops in gravitational field, we assumed that the detachment happens when the drop shape becomes unstable. In other words, the drop breakup is related to a transition from stable to unstable dynamic equilibrium, rather than to a lack of equilibrium (i.e., misbalance of the acting forces). The basic model assumption is that, at the moment of breakup, the hydrodynamic ejection force, F_h, acting on the drop is equal to the critical capillary force that corresponds to the stability−instability transition in the drop profile (eq 5.9). This leads to a mathematical formula (eq 5.12) that expresses the condition for drop detachment. Further, this expression is applied to predict the mean size of the obtained drops in regimes of constant flow rate (eq 5.18 and Figure 14) and constant transmembrane pressure (eq 5.28 and Figure 16). It turns out that the production of monodisperse drops at pressures slightly greater than the critical one corresponds to a working regime near the minima of the curves in Figure 16 (see sections 5.4 and 5.5). Theoretically, the positions of the latter minima are insensitive to the variation of the interfacial tension and to the increase of viscosity of the inner (oil) phase at viscosity ratios in the range $0 < \eta_b/\eta_a < 0.3$, in full agreement with the experimental findings. In addition, the transition from unimodal to bimodal drop size distribution upon increase of the transmembrane pressure (or flow rate) can be interpreted in terms of the transition from the "dripping" to the "jetting" mechanism of drop breakup (section 6).

Our results could be useful for a deeper understanding of the physicochemical factors and mechanisms that influence the process of membrane emulsification and could be helpful for prediction and control of the mean size and polydispersity of the drops in the produced emulsions.

Acknowledgment. This work was supported in part by the EC Inco-Copernicus Project, No. IC15CT980911. Partial support of COST Action D43 is acknowledged. The authors are grateful to Dr. Volker Schröder for the helpful discussions.

Appendix A. Calculation of $V_{max}(\lambda)$ and $f_h(\alpha)$

Calculation of the Dimensionless Maximum Drop Volume, $\tilde{V}_{max}$. For this goal, one can use accurate interpolation formulas from ref 40. Note that, in view of eq 5.13, smaller λ corresponds to bigger drops.

(i) For the biggest drops ($\lambda \leq 0.101570$), one can use the expression

$$\tilde{V}_{max} = (2\pi f_d \lambda)^{3/2} \quad \text{(A.1)}$$

where f_d is given by the Gunde−Hartland asymptotic expansion:

$$f_d = 0.99998 - 1.561285\lambda + 3.131809\lambda^2 - 4.048916\lambda^3 + 2.849794\lambda^4 - 0.761799\lambda^5 \quad \text{(A.2)}$$

(ii) For drops of intermediate size ($0.101570 \leq \lambda \leq 0.341116$), one can use the expression[40]

$$\tilde{V}_{max} = -0.25713558 \times 10^{-13} + 1.8130156\lambda + 36.028621\lambda^2 - 196.02815\lambda^3 + 706.78973\lambda^4 - 1577.8383\lambda^5 + 2603.8524\lambda^6 - 3316.2890\lambda^7 + 2376.3198\lambda^8 \quad \text{(A.3)}$$

(iii) For the smallest drops ($0.341116 \le \lambda \le 0.976264$), one can use the expression[40]

$$\tilde{V}_{max} = -6.4649722 + 92.566656\lambda - 509.65058\lambda^2 + 1642.2681\lambda^3 - 3104.5603\lambda^4 + 3512.2924\lambda^5 - 2175.1711\lambda^6 + 594.94227\lambda^7 - 29.400607\lambda^8 \quad (A.4)$$

From eq 5.13 we obtain that $\lambda > 0.976264$ corresponds to $d_d/d_p < 0.6354$; for the processes investigated by us, smaller drops do not represent physical interest.

Hydrodynamic Force Coefficient, f_h. To calculate this coefficient, we will use expressions derived in ref 15 for protrusion angles in the range $150° \le \alpha \le 180°$, which corresponds to $d_d/d_p \ge 1.9914$ (see eqs 5.13 and 5.15). Thus, $f_h(\alpha)$ is given by the expression[15]

$$f_h(\alpha) \equiv f_{a,0}(\alpha) + \frac{\eta_b}{\eta_a}[f_b(\alpha) + f_{ab}(\alpha)] \quad (A.5)$$

where[15]

$$f_{a,0}(\alpha) \approx 15.4891 - 1.5710\cos(2\alpha) - 3.0621\cos^2(2\alpha) + 2.1847\cos^3(2\alpha) \quad (A.6)$$

$$f_{ab}(\alpha) \approx \frac{9}{2}\pi\xi\left(1 + \frac{1 - 433.64\xi}{12.063 + 9255.6\xi}\right),\ \xi \equiv (1 + \cos\alpha)\sin\alpha \quad (A.7)$$

$$f_b(\alpha) = f_{wedge} - 3\pi\cot\left(\frac{\alpha}{2}\right)\left\{1 + 0.94095\left[1 - \exp\left(-25.822\cot\frac{\alpha}{2}\right)\right]\right\} \quad (A.8)$$

$$f_{wedge} \approx 6\pi\cot\left(\frac{\alpha}{2}\right)\left[0.79381 - \ln(\pi - \alpha) + \frac{(\pi - \alpha)^2}{24} - \frac{(\pi - \alpha)^4}{1440}\right] \quad (A.9)$$

The accuracy of eqs A.6−A.9 is given in ref 15.

Appendix B. Calculation of $\pi_0(L/r_p)$

To calculate the pressure along the axis of revolution in the inner phase "a" (Figure 13), we will use the *z*-component of the momentum balance equation. In terms of dimensionless variables, the latter can be expressed in the form[15]

$$\frac{1}{\tilde{r}}\frac{\partial}{\partial\tilde{r}}\left(\tilde{r}\frac{\partial\tilde{w}_a}{\partial\tilde{r}}\right) + \frac{\partial^2\tilde{w}_a}{\partial\tilde{z}^2} = \frac{\partial\tilde{p}_{a,0}}{\partial\tilde{z}} \quad (B.1)$$

where the dimensionless coordinates are $\tilde{r} = r/r_p$ and $\tilde{z} = z/r_p$, and the dimensionless pressure, $\tilde{p}_{a.0}$, is defined by eq 5.23. Let us integrate eq B.1 along the axis of revolution ($r = 0$) from $z = -L$ to the drop apex (Figure 13):

$$\int_{-L/r_p}^{apex}\frac{1}{\tilde{r}}\frac{\partial}{\partial\tilde{r}}\left(\tilde{r}\frac{\partial\tilde{w}_a}{\partial\tilde{r}}\right)d\tilde{z} + \left.\frac{\partial\tilde{w}_a}{\partial\tilde{z}}\right|_{ap} - \left.\frac{\partial\tilde{w}_a}{\partial\tilde{z}}\right|_{-L/r_p} = \tilde{p}_{a,0}|_{ap} - \pi_0 \quad (B.2)$$

As usual, the subscript "ap" denotes that the respective quantity should be estimated at the drop apex. For the position vector **r** situated at the apex, the terms with p_a in the left- and right-hand sides of eq 5.23 cancel each other, and one obtains

$$\left.\tilde{p}_{a,0}\right|_{ap} = \frac{2r_p}{\nu_m}\left.\frac{\partial w_a}{\partial z}\right|_{ap} \quad (B.3)$$

Substituting eq B.3 into eq B.2, we derive

$$\pi_0 = -\int_{-L/r_p}^{apex}\frac{1}{\tilde{r}}\frac{\partial}{\partial\tilde{r}}\left(\tilde{r}\frac{\partial\tilde{w}_a}{\partial\tilde{r}}\right)d\tilde{z} + \left.\frac{\partial\tilde{w}_a}{\partial\tilde{z}}\right|_{ap} + \left.\frac{\partial\tilde{w}_a}{\partial\tilde{z}}\right|_{-L/r_p} \quad (B.4)$$

From eqs D.16 and D.17 in ref 15 (Appendix D), it follows

$$\pi_0 = -\int_{-L/r_p}^{apex}\frac{1}{\tilde{r}}\frac{\partial}{\partial\tilde{r}}\left(\tilde{r}\frac{\partial\tilde{w}_a}{\partial\tilde{r}}\right)d\tilde{z} + \left.\frac{\partial\tilde{w}_a}{\partial\tilde{z}}\right|_{-L/r_p} - 2\sin\alpha(1 + \cos\alpha) \quad (B.5)$$

Finally, with the help of eqs D.12 and D.21 in ref 15 (Appendix D), we obtain

$$\pi_0 = \frac{8}{3}\int_{-L/r_p}^{apex}\frac{\partial^3\psi_a}{\partial\tilde{r}^3}d\tilde{z} - 2\left.\frac{\partial^2\psi_a}{\partial\tilde{r}\partial\tilde{z}}\right|_{-L/r_p} - 2\sin\alpha(1 + \cos\alpha) \quad (B.6)$$

where ψ_a is the dimensionless stream function defined and calculated in ref 15. From the numerical solution for ψ_a, the derivatives and the integral in eq B.6 have been numerically calculated. The results are shown in Figure 15, where $z \equiv -L$.

LA702306F